Radio Science, Volume 32, Number 2, Pages 411–423, March–April 1997

Sub-Fresnel-scale vertical resolution in atmospheric profiles from radio occultation

E. Tuna Karayel and David P. Hinson

Center for Radar Astronomy, Stanford University, Stanford, California

Abstract. We have investigated the vertical resolution that can be achieved in atmospheric profiles retrieved from radio occultation measurements. The results are based on forward simulations of radio wave propagation through model atmospheres using the multiple phase-screen method. We find that profiles retrieved through Abel inversion, the standard algorithm derived from geometrical optics, have a vertical resolution that is diffraction-limited, as expected. To overcome this limitation, we have developed an advanced retrieval algorithm, which is based on scalar diffraction theory and properly accounts for diffraction effects. We demonstrate that the method is capable of retrieving accurate refractivity profiles at sub-Fresnel-scale resolution for Mars- and Earth-like atmospheres. It also provides a natural means for deciphering multipath propagation effects. The method seems capable of enhancing resolution by a factor of 10 beyond the diffraction limit. In one simulation involving an Earth-like model atmosphere the algorithm successfully retrieved a profile in which the refractive index changed by 10^{-5} over a vertical scale of 250 m. The maximum vertical gradient of refractive index within this small-scale feature was about 0.8×10^{-7} m^{-1}. For comparison, critical refraction occurs for a gradient of about 1.6×10^{-7} m^{-1}. The feature was embedded in a smooth refractive index profile at the level where the pressure and mean refractive index were 42 kPa and 1.00013, respectively. Total refractive bending for a ray that grazed this level was 0.01–0.02 rad.

Introduction

Radio occultation experiments have played a prominent role in solar system exploration for nearly 30 years. They have contributed uniquely to studies of the atmospheres of terrestrial planets (Venus and Mars), gas giants (Jupiter, Saturn, Uranus, and Neptune), and outer-planet satellites (Io, Titan, and Triton). This experience has yielded an accurate and reliable technique for remote sensing [e.g., *Tyler*, 1987].

The conventional algorithm for retrieving atmospheric profiles from radio occultation measurements, Abel inversion, is based on the laws of geometrical optics [*Fjeldbo et al.*, 1971]. The method ignores diffraction effects, so that retrieved profiles have a vertical resolution that is diffraction-limited to about the diameter of the first Fresnel zone [e.g., *Fjeldbo and Eshleman*, 1969]. When defocusing is negligible, this is roughly $2(\lambda D)^{1/2}$, where λ is the wavelength of radiation and D is the spacecraft-to-planet distance. In typical experiments, $2(\lambda D)^{1/2} \approx 1$ km, much smaller than an atmospheric scale height.

Fresnel-scale vertical resolution, though impressive, is not sufficient for some objectives, and no method previously existed for overcoming the basic diffraction limit inherent to Abel inversion. With this motivation we have developed the first data inversion algorithm that, by properly accounting for diffraction effects, allows retrieval of atmospheric structure at sub-Fresnel-scale resolution in atmospheres as dense as those of Mars and Earth. Potential applications include studies of the near-surface boundary layer of Mars in the upcoming Mars Global Surveyor (MGS) Mission [*Tyler et al.*, 1992] and of the ionospheres of Jupiter and Io through distant radio occultations of the Galileo orbiter [*Howard et al.*, 1992]. In addition, the radio occultation technique is now being applied for the first time to Earth's atmosphere using signals transmitted by satellites of the Global Positioning System (GPS) and received by another satellite orbiting at a lower altitude [*Kursinski et al.*, 1996; *Ware et al.*, 1996]. More detailed investigations of fine structure near the tropopause and of the boundary layer adjacent to the surface should now be feasible.

Paper number 96RS03212.
0048-6604/97/96RS-03212$11.00

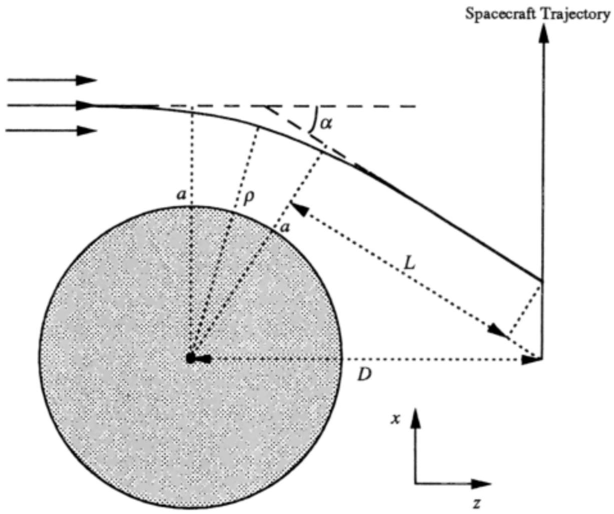

Figure 1. Idealized radio occultation experiment geometry. The ray path (solid line) and asymptotes (long-dashed lines) are shown for a ray with periapse ρ and impact parameter a. Refractive bending produces a deflection between the ray asymptotes by an angle α. The spacecraft is moving along the x direction, perpendicular to the incoming rays, at a distance D behind the planet. The coordinate origin is at the center of the planet.

As part of this research, we conducted accurate numerical simulations of radio occultation experiments. The simulated data were essential to developing and testing our advanced retrieval algorithm, but the forward simulations are potentially important for another reason. To date, the GPS receiver carried by the MicroLab 1 satellite has generally failed to acquire data in the lowest several kilometers above Earth's surface, except at high latitudes [*Kursinski et al.*, 1996; *Ware et al.*, 1996]. The receiver is apparently not capable of handling the complex signal dynamics, including diffraction and multipath, associated with abrupt, water-induced, vertical variations in refractive index. Simulations like the ones presented here can guide the design of advanced receivers for future satellites.

The paper is organized as follows. We begin by describing the conventional Abel-inversion algorithm. After introducing the atmospheric models used in our numerical simulations, we explain an accurate method, based on a multiple phase-screen (MPS) representation, for modeling the propagation of electromagnetic waves through a planetary atmosphere. The use of multiple phase screens represents a significant improvement over single-screen models of planetary atmospheres used in previous forward simulations [e.g., *Haugstad*, 1978; *French and Lovelace*, 1983]. We then apply the MPS method to simulate occultation measurements for Mars- and Earth-like model atmospheres, and we address the question of vertical resolution through Abel inversion of the simulated data. The vertical resolution of the retrieved profiles is shown to be diffraction-limited, as expected. Finally, we present a more general retrieval algorithm, which can overcome this limitation by properly accounting for diffraction effects, and we discuss its limitations.

Propagation and Retrievals Within Geometrical Optics

The wavelength λ of signals used in typical radio occultation experiments is 1–20 cm, much smaller than the characteristic spatial scale of the atmospheric structure being measured. Consequently, the traditional method for retrieving atmospheric profiles from these measurements is based on the theory of geometrical optics, the limiting form of Maxwell's equations when $\lambda \to 0$ [*Born and Wolf*, 1986, pp. 109–132]. This section introduces the geometrical optics framework and briefly describes the basic retrieval algorithm, known as Abel inversion.

Figure 1 shows the experiment geometry. A transmitter radiates an unmodulated, monochromatic signal, which passes through a planetary atmosphere and is received by a spacecraft moving along its trajectory at a distance D behind the limb. In the limit where $\lambda \to 0$, the electromagnetic radiation can be described geometrically as following distinct ray paths. The rays arriving at the planet's atmosphere are nearly parallel to each other (i.e., the wave fronts are nearly planar) due to the relatively large transmitter-to-planet distance. Refractive index generally decreases with radius in the neutral atmosphere, which causes a ray to bend by an angle α toward the planet. The closest approach distance of the ray to the center of the planet is defined as the ray periapse ρ. If the refractive index varies only with radius, both ray asymptotes will be at the same distance from the center of the planet. This distance is defined as the impact parameter a.

Throughout this paper we will use a cylindrical model for the planet's atmosphere such that there is no variation in the y direction, perpendicular to the plane of Figure 1. This simplifies the numerical simulations and reduces computation time. For a spherically symmetric atmosphere, the only variations in the y direction would be the result of limb curvature and would not cause any significant change in our results.

The spacecraft makes a series of phase measurements, $\phi(x)$, of the electromagnetic field as it moves along the observation line, which is assumed to be perpendicular to the incoming rays for simplicity (Figure 1). The derivative of ϕ with respect to x is determined by the local orientation of the wave fronts arriving at the spacecraft, which leads to the relation

$$\alpha = \sin^{-1}\left(\frac{-\lambda}{2\pi}\frac{d\phi}{dx}\right). \tag{1}$$

The impact parameter can then be obtained from the experiment geometry:

$$a = D \sin \alpha + x \cos \alpha. \tag{2}$$

Equations (1)–(2) allow phase measurements to be reduced to bending angle as a function of impact parameter.

Conversely, the phase ϕ and amplitude A can be obtained from $\alpha(a)$. From (1),

$$\phi(x) = \frac{2\pi}{\lambda}\int_x^\infty \sin \alpha \, dx \tag{3}$$

when $\phi(\infty)$ is set to zero as a reference. To calculate the amplitude, we compare the distance between two rays before entering the atmosphere, Δa, with their separation at the observation line, $\Delta x \cos \alpha$. The amplitude observed by the spacecraft is

$$A(x) = \left(\frac{1}{\cos \alpha}\frac{da}{dx}\right)^{1/2}, \tag{4}$$

where the incoming wave fronts are assumed to have unit amplitude. Substitution from (2) yields the geometrical optics result for $A(x)$ in the cylindrical geometry:

$$A(x) = \frac{1}{\left(1 - L\dfrac{d\alpha}{da}\right)^{1/2}}, \tag{5}$$

where $L \equiv D \cos \alpha - x \sin \alpha$ (cf. Figure 1). In addition to changing the signal amplitude, refractive focusing or defocusing also causes distortion of the Fresnel zone to a noncircular shape [e.g., *Haugstad*, 1978]. Its radius in the z direction becomes

$$r_f = \frac{(\lambda D)^{1/2}}{\left(1 - L\dfrac{d\alpha}{da}\right)^{1/2}}. \tag{6}$$

We will refer to r_f as the Fresnel scale for short.

For a spherically or cylindrically symmetric atmosphere the geometrical-optics relationship between $\alpha(a)$ and refractive index as a function of radius, $\mu(r)$, takes the form of an Abel transform [*Fjeldbo et al.*, 1971]:

$$\alpha(a) = -2a\int_\rho^\infty \frac{d \ln \mu}{dr}\frac{dr}{[(\mu r)^2 - a^2]^{1/2}}. \tag{7}$$

For a specific ray with asymptote a_1 and periapse ρ_1, inversion of (7) yields

$$\pi \ln \mu(\rho_1) = \int_{a_1}^\infty \frac{\alpha(a)}{(a^2 - a_1^2)^{1/2}}\, da \tag{8}$$

where

$$\rho_1 = \frac{a_1}{\mu(\rho_1)}. \tag{9}$$

Thus a refractive index profile can be retrieved from $\alpha(a)$ through use of (8)–(9). For a general discussion of the Abel transform and its properties, see *Bracewell* [1986, pp. 262–266]. The vertical resolution of profiles retrieved through Abel inversion is roughly $2r_f$ [cf. *Hinson and Magalhães*, 1991].

Knowledge of the refractive index profile together with the atmospheric composition yields the mass density profile. Pressure and temperature profiles can then be obtained by assuming hydrostatic balance and using an equation of state [e.g., *Fjeldbo and Eshleman*, 1968].

An exact Abel transform pair $[\alpha(a), \mu(r)]$ appropriate to represent planetary atmospheres is known to exist [*Eshleman*, 1973, 1989]:

$$\alpha = Q\left(\frac{R}{a}\right)^q, \tag{10}$$

$$(1 + \nu)^q \ln (1 + \nu) = \left(\frac{R}{r}\right)^q \tag{11}$$

where $\nu \equiv \mu - 1$ is refractivity, q and R are constants, and

$$Q \equiv 2\pi^{1/2}\frac{\Gamma[(q+1)/2]}{\Gamma(q/2)}. \tag{12}$$

With appropriate choices for q and R the expression for $\nu(r)$ corresponds to a nearly isothermal atmosphere with scale height $H \approx R/q$. These formulas will be used to test the accuracy of forward simula-

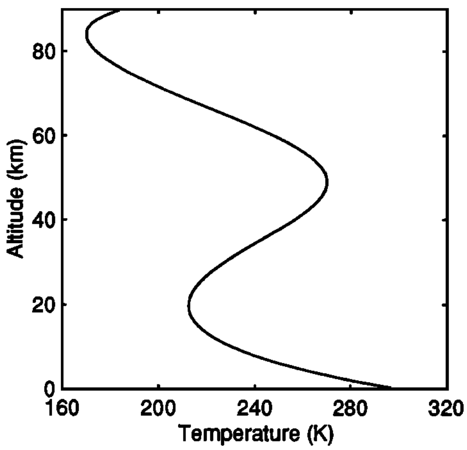

Figure 2. Temperature profile used to represent the background terrestrial atmosphere. Temperature was calculated from refractivity by assuming a dry atmosphere and using the hydrostatic equation and the ideal gas law. In calculating altitude the radius of Earth is assumed to be 6378 km.

tions and to represent the background structure in the atmosphere of Mars.

Atmospheric Models

The atmospheric models used in our numerical simulations consist of a small-scale structure of variable size superimposed on a smoothly varying background. The refractivity profile is given by

$$\nu(r) = \nu_0(r) + \nu_1(r) \tag{13}$$

where ν_0 is the background structure and ν_1 is the small-scale variation. To simplify our initial simulations, we used (11) to represent $\nu_0(r)$ on Mars. We required a more accurate model for $\nu_0(r)$ in the terrestrial atmosphere, which we obtained by fitting a seventh-order polynomial in $\log_{10} \nu$ versus height to a standard model atmosphere for June at 40°N latitude [*Houghton*, 1977, p. 173]. The temperature profile corresponding to this fit is shown in Figure 2.

The small-scale feature takes the form

$$\nu_1(r) = \begin{cases} 0, & r - r_0 > \dfrac{\Delta r}{2} \\ \dfrac{\nu_s}{2} \left\{1 - \sin\left[\dfrac{\pi(r - r_0)}{\Delta r}\right]\right\} & |r - r_0| < \dfrac{\Delta r}{2} \\ \nu_s, & r - r_0 < -\dfrac{\Delta r}{2} \end{cases} \tag{14}$$

It consists of a constant refractivity ν_s added below $r_0 - \Delta r/2$ and a half period sinusoidal transition between $r_0 - \Delta r/2$ and $r_0 + \Delta r/2$. In both the Martian and terrestrial models the refractivity and its vertical gradient are continuous.

Figure 3 shows the effect of the small-scale structure on the temperature profile for the terrestrial case. The corresponding refractivity profile closely resembles what is commonly observed in radiosonde measurements over Hilo, Hawaii, where a sharp change in the abundance of water vapor causes an abrupt change in refractivity at an altitude of about 2–4 km above the surface (K. R. Hardy, personal communication, 1995). Our model differs in that the change in refractivity is attributed entirely to vertical variations of temperature in a dry atmosphere (Figure 3). As the fundamental quantity retrieved from radio occultation data is refractive index versus radius, this simplification had no effect on our basic results and conclusions.

An example for Mars is shown in Figure 4. This small-scale structure in refractivity corresponds to a temperature inversion, whereas the pressure profile is not noticeably affected by it (Figure 5). This type of model can be used to represent sharp temperature inversions, which have been observed just above the polar caps of Mars [e.g., *Lindal et al.*, 1979, Figure 3] and are also expected to occur in the nighttime boundary layer [e.g., *Zurek et al.*, 1992, Figure 15].

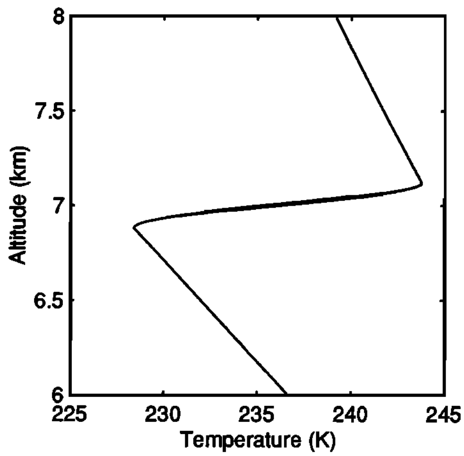

Figure 3. Terrestrial temperature profile corresponding to a small-scale sinusoidal feature (cf. equation (14)) superimposed on the background structure in Figure 2. In this example, the feature is centered at $r_0 = 6385$ km (an altitude of 7 km) with $\nu_s = 10^{-5}$ and $\Delta r = 250$ m. At this radius, $\nu_0 = 1.3 \times 10^{-4}$, and the pressure is 42 kPa.

A planetary surface will produce something resembling a knife-edge diffraction pattern in a radio occultation experiment. This can sometimes dominate the diffractive effects caused by small-scale atmospheric structure, particularly if the structure is located within a few Fresnel zones of the surface and the atmosphere is tenuous. Hence, in the interest of concentrating on the atmospheric effects, we decided not to include a planetary surface in either the terrestrial or Martian simulations. However, we anticipate that with further development the retrieval algorithm described below will be capable of simultaneously resolving diffractive effects caused by planetary surfaces and those caused by atmospheric structures.

Scalar Diffraction Theory: Forward Propagation

This section describes an alternative method for modeling the propagation of electromagnetic (EM) waves through an inhomogeneous medium. This method accounts for effects that arise when $\lambda \neq 0$ and is thus more general than geometrical optics. We restrict attention to the case where $\alpha \ll 1$ and consider atmospheres with appreciable variations in refractive index on spatial scales, ℓ, such that $\ell \gg \lambda$. Under these conditions we can adopt the parabolic approximation to the EM wave equation, and we can treat the electric and magnetic fields of the wave as scalars, since polarization effects are negligible [*Tatarskii*, 1971]. EM wave propagation can be simulated accurately for this case using the multiple phase-screen (MPS) method [*Knepp*, 1983; *Martin and Flatté*, 1988].

The basic idea behind the MPS method is to model the atmosphere as a series of thin phase screens separated by vacuum and to propagate an EM wave through these screens one by one (Figure 6). The initial direction of propagation is taken to be the z direction. The atmosphere is divided into layers that extend in the x direction. Each layer is replaced by a phase screen that represents the geometrical optics phase delay that would be caused by that layer. This phase shift is approximated as the path integral of refractivity along the z direction over the width of the layer, with the result multiplied by the vacuum wave number $k \equiv 2\pi/\lambda$. For layer n centered at $z = z_n$ with a width of Δz the phase shift is

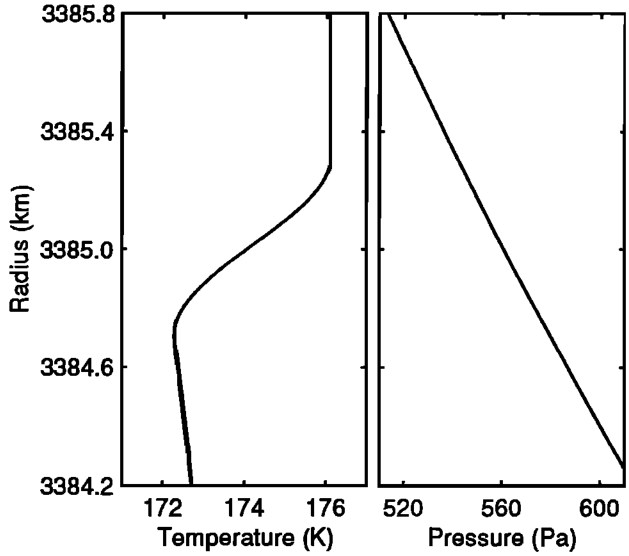

Figure 5. Martian temperature and pressure profiles corresponding to the refractivity profile in Figure 4. We calculated these profiles from the hydrostatic equation and the ideal gas law using the atmospheric composition measured by the Viking landers [*Owen*, 1992].

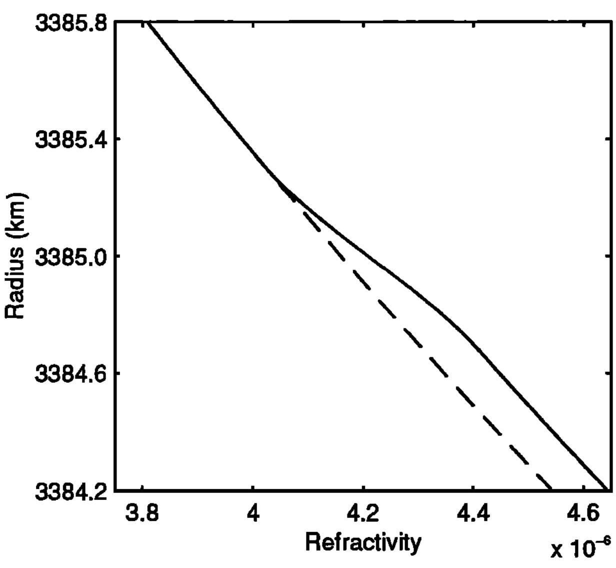

Figure 4. Martian refractivity profile used in forward simulations. The total refractivity (solid line) consists of a power law model for the background structure (dashed line) with a small-scale sinusoidal feature superimposed. In this example, q = 375, R = 3275 km, and the feature is centered at r_0 = 3385 km, the mean radius of Mars, with $\nu_s = 10^{-7}$ and Δr = 630 m. This model resembles Mars in that $\nu \sim 4 \times 10^{-6}$, $H \sim 9$ km, and the pressure is 560 Pa at r = 3385 km [cf. *Fjeldbo and Eshleman*, 1968].

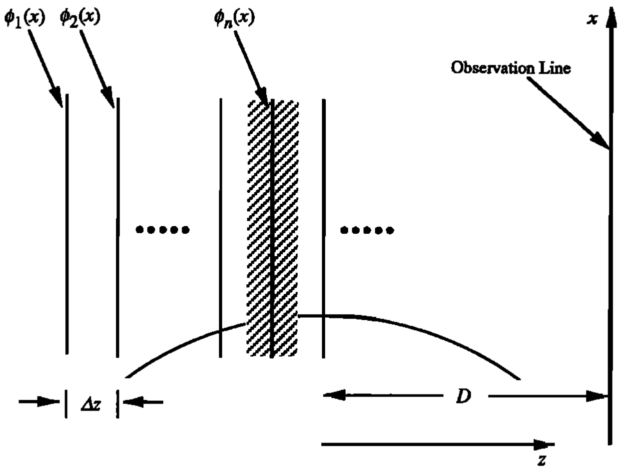

Figure 6. Multiple phase-screen model. Shaded area indicates portion of atmosphere represented by phase screen ϕ_n. The distance between the central screen and the observation line is D.

$$\phi_n(x) = k \int_{z_n-\Delta z/2}^{z_n+\Delta z/2} [\mu(x, z) - 1]\, dz. \tag{15}$$

Let $u(x, z_n^-)$ represent the complex electric field just prior to screen n and $u(x, z_n^+)$ represent the field emerging from it. The relationship between the two is

$$u(x, z_n^+) = u(x, z_n^-) \exp [i\phi_n(x)]. \tag{16}$$

The immediate effect of each screen is to modulate the phase but not the amplitude of an EM wave passing through it. However, an interference pattern develops with distance as the phase-modulated wave propagates away from the screen, causing additional diffractive variations in amplitude and phase.

Propagation between adjacent screens (i.e., through vacuum) can be handled accurately and efficiently by representing the field as a spectrum of plane waves. This is accomplished by taking the transverse Fourier transform of $u(x, z_n^+)$ [*Goodman*, 1968, pp. 48–51]:

$$U(k_x, z_n^+) = \int_{-\infty}^{\infty} u(x, z_n^+) e^{-ik_x x}\, dx \tag{17}$$

where k_x is the wave number in the x direction. The corresponding wave number in the z direction is

$$k_z = (k^2 - k_x^2)^{1/2}. \tag{18}$$

Each Fourier component experiences a different phase shift in propagating to the next screen:

$$U(k_x, z_{n+1}^-) = U(k_x, z_n^+) \exp (ik_z \Delta z) \tag{19}$$

where Δz is the distance between adjacent screens. The field just before screen $n + 1$ is then obtained by combining the phase-shifted Fourier components (i.e., by taking the inverse Fourier transform):

$$u(x, z_{n+1}^-) = \frac{1}{2\pi} \int_{-\infty}^{\infty} U(k_x, z_{n+1}^-) e^{ik_x x}\, dk_x. \tag{20}$$

Equations (16), (17), (19), and (20) represent the four basic steps used to propagate the field through one "element" of the MPS structure. The field emerging from the occulting atmosphere can be calculated by repeating these steps successively for all screens starting with the planar wave front arriving at the first screen. Vacuum propagation from the last atmospheric phase screen to the observation line is computed through one final application of (17)–(20), but with Δz replaced by the distance to the observation line. Note that (17)–(20) are equivalent to a standard Huygens-Fresnel diffraction integral [*Goodman*, 1968, pp. 30–56].

We tested the accuracy of the MPS method by simulating propagation through a power law model atmosphere with $q = 375$ and $R = 3275$ km but no small-scale structure (cf. Figure 4). (The simulations are described in more detail in the next section.) We then compared the results with geometrical optics predictions, which can be calculated analytically for this case (cf. equation (10)) and should be accurate in the absence of small-scale atmospheric structure. The results from the two methods agree closely. The amplitudes differ by less than one part in 10^7. The phase difference is less than 2×10^{-4} rad compared to a total phase shift of $\sim 100\ \pi$ rad. This confirms the accuracy of our MPS calculations.

Effect of Diffraction on Abel Inversion

We are now in a position to illustrate diffraction effects as they occur in atmospheric occultations and to quantify the corresponding errors that appear in profiles retrieved through Abel inversion. This will be accomplished by first using the MPS method to calculate the amplitude and phase that would be observed during a radio occultation by an atmosphere containing small-scale structure. We then retrieve atmospheric profiles from the simulated data through

Abel inversion. The performance is evaluated by comparing the retrievals with the actual structure used in the forward simulations.

We conducted a series of MPS simulations for Mars-like model atmospheres using four different values for Δr (630, 250, 100, and 40 m). Parameters q, R, r_0, and ν_s were held fixed at the values used in Figure 4. We set $D = 1750$ km and $\lambda = 3.5$ cm, which correspond to the radio occultations planned for the MGS Mission [*Tyler et al.*, 1992].

We used 257 phase screens with a separation Δz of 7 km to represent the occulting atmosphere. This model can accurately predict effects caused by atmospheric structure on scales as small as $\ell \sim 2(\lambda \Delta z)^{1/2} \sim 30$ m [cf. *Hinson and Magalhães*, 1991]. Each phase screen consists of 32,768 discrete samples with a separation Δx of 5 m. With this sample spacing, aliasing does not occur until a wave front is tilted relative to a phase screen by an angle of more than $\lambda/(2\Delta x) \sim 3.5 \times 10^{-3}$ rad. This angle exceeds the refractive bending caused by the atmosphere of Mars by more than an order of magnitude.

Because we are using discrete Fourier transforms in the MPS calculations, each phase screen is implicitly periodic in the x direction [*Brigham*, 1974]. In this example, the period is 32,768 samples. The screens were designed to avoid artifacts produced by this effect. The central 25,000 samples were computed directly from (11), (14), and (15), while 7,768 samples near the screen edges were chosen to produce a smooth transition from one end of the screen to the other. This guard band suppresses the diffraction effects that would result from an abrupt transition. It also acts as a buffer against energy leaving one end of the screen and entering at the other.

Figure 7 shows the amplitude of the field along the observation line from the MPS calculations. Note that defocusing by the background atmosphere has decreased the average amplitude by about 2%, so that $r_f \approx 240$ m, not appreciably different than its undistorted size (cf. equations (5) and (6)). When $\Delta r = 630$ m, the scattered field is nearly free of diffraction and the amplitude variations are caused primarily by refractive effects. Diffraction effects appear in the form of damped oscillations when the structure size is 250 m or smaller. These oscillations become more prominent as Δr decreases. Although the small-scale structures are located at a radius of 3385 km, the diffraction pattern they produce is centered a few hundred meters lower. This shift is the result of refraction by the background atmospheric structure.

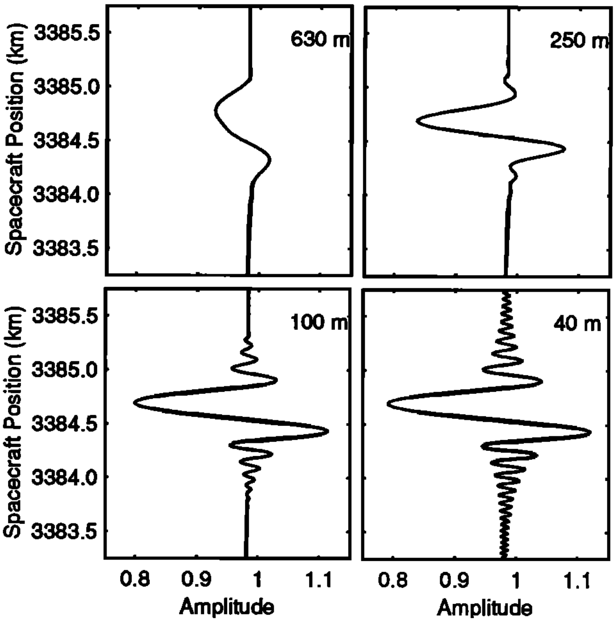

Figure 7. MPS calculations of received signal amplitude for four different structure sizes (Δr = 630, 250, 100, and 40 m). The 250-, 100-, and 40-m structures cause noticeable diffraction effects.

Similar diffraction effects are present in the phase of the received signal. However, these are difficult to display because the phase oscillations due to diffraction are small compared to the phase shift introduced by the background structure ($\sim$100 π rad). For this reason we provide plots of signal frequency (Figure 8), which is proportional to the derivative of phase and therefore emphasizes the diffraction effects.

Temperature profiles obtained through Abel inversion of the simulated phase data are shown in Figure 9. (Retrieved refractivity profiles exhibit similar behavior.) The 630-m structure is retrieved accurately, while structure of Fresnel scale or smaller is corrupted significantly. The Abel inversion method attributes each phase oscillation in the received signal to a distinct structure in the atmosphere, with the result that the three retrievals corresponding to 40- to 250-m scales contain temperature oscillations that resemble the underlying diffraction patterns. Moreover, the retrievals fail to resolve sharp temperature gradients when these occur over scales of Fresnel-zone size or smaller. These results illustrate the diffraction limit to resolution inherent to Abel inversion.

For future reference, we also ran MPS simulations for the terrestrial atmosphere using the model shown

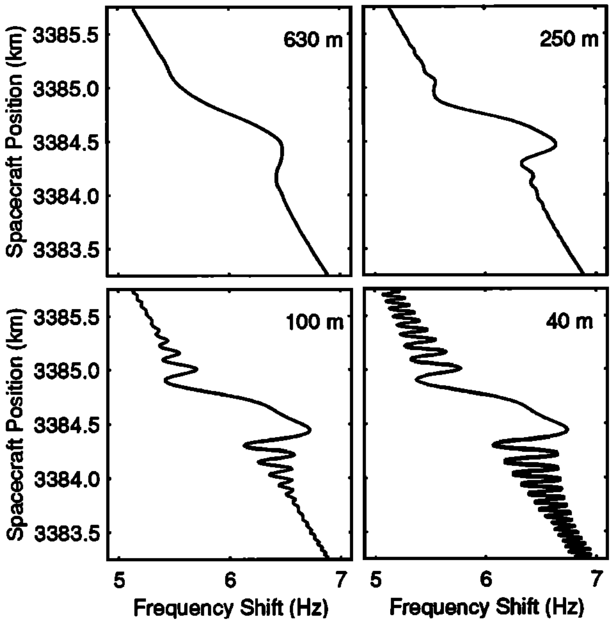

Figure 8. Frequency shift of the scattered field corresponding to the amplitude patterns shown in Figure 7. The spacecraft is assumed to be moving with a velocity of 1 km s^{-1} along the observation line. Diffraction effects are evident for the 250-, 100-, and 40-m structures.

in Figure 3. We used 449 phase screens with a separation Δz of 6.25 km. Each screen consisted of 262,144 samples (including the guard band) with a separation Δx of 1 m. We set $D = 2000$ km and $\lambda = 20$ cm, which approximates an experiment involving one satellite in "low-Earth" orbit receiving signals radiated by GPS satellites [*Kursinski et al.*, 1996; *Ware et al.*, 1996]. The Fresnel scale ($r_f = 360$ m) is significantly larger than the small-scale structure in the model ($\Delta r = 250$ m). Figure 10 shows MPS calculations of signal amplitude along the observation line, which exhibit pronounced diffraction effects. Most of the diffraction effects are confined to the observation position range of 6360–6370 km. Note also the presence of more subtle oscillations in amplitude well below the main diffraction pattern. These are artifacts of the MPS simulation caused by the representation of the atmosphere as a series of discrete thin screens. We performed additional simulations using various values for Δz and found that these artifacts can be reduced by decreasing the screen separation. With our current choice of 6.25 km the artifacts are much smaller than the main diffraction pattern so that their effect is insignificant (see below).

Scalar Diffraction Theory: Retrieval Algorithms

The method of Abel inversion is based on geometrical optics [*Fjeldbo et al.*, 1971], so it is not surprising that the resulting atmospheric profiles have a diffraction-limited vertical resolution of about $2r_f$. However, this limitation on resolution is not fundamental and can be overcome by using a retrieval method that accounts for diffraction effects [cf. *Cohen*, 1969]. One such method is based on the Fourier Diffraction Theorem [*Kak and Slaney*, 1988, pp. 218–234]. Although it has a solid theoretical basis, it works only for extremely tenuous atmospheres (e.g., Pluto). Discussion of that method is therefore not included here. In this section we introduce a far more general method, dubbed "back-propagation," and demonstrate that it works remarkably well for atmospheres as dense as Earth's.

The back-propagation method proceeds as follows. We begin by taking the Fourier transform of $u(x, D)$, the complex field along the observation line, to obtain the plane wave spectrum $U(k_x, D)$ (cf. equation (17)). Next, $U(k_x, D)$ is propagated backward in the z direction by a distance $D - b$ through use of (19):

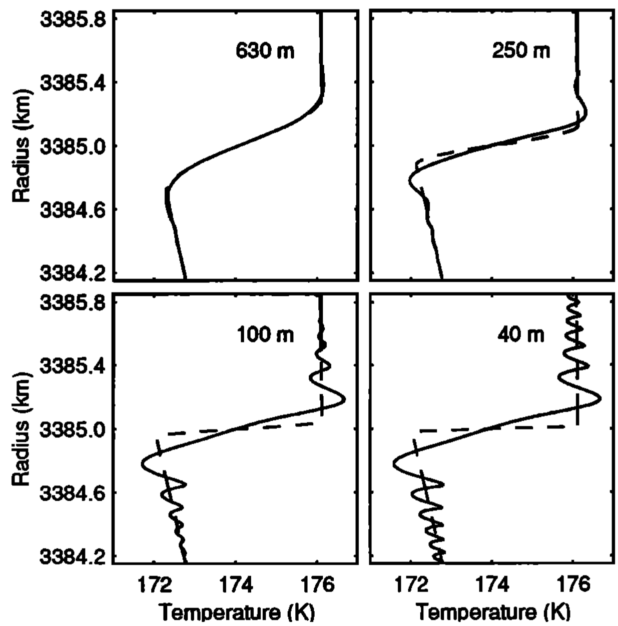

Figure 9. Temperature retrievals based on Abel inversion of simulated data. Dashed curves show atmospheric models used in the forward simulations; solid curves were obtained through Abel inversion.

$$U(k_x, b) = U(k_x, D) \exp[-ik_z(D - b)]. \quad (21)$$

An inverse Fourier transformation of the left-hand side yields $u(x, b)$ (cf. equation (20)). By using scalar diffraction theory to implement the backward propagation our goal is to remove diffraction effects from the data, yielding an equivalent data set for which the effective value of r_f has been reduced to zero. In cases where this backward propagation step is not sufficient for completely removing diffraction effects, the adjustable parameter b can still be tuned to a value where they are minimized. We discovered empirically that an advantageous choice for b corresponds to $L = 0$ in (5). This is the geometrical optics prediction for the location of unit amplitude assuming vacuum propagation. From Figure 1 we see that $L = 0$ when $b = a \sin \alpha$. The optimum choice for b generally satisfies $b \ll D$.

The next step in the back-propagation method is to compute bending angle versus impact parameter from $u(x, b)$. This can be done with (1) and (2); the only modification needed is to replace D with b in the latter. Atmospheric profiles are then obtained as in standard Abel inversion (cf. equations (8) and (9)). The back-propagation method described here, while not fundamentally new, represents a significant extension of previous inversion algorithms used in atmospheric occultations.

This back-propagation method is a simple adaptation of an approach to data inversion developed previously by *Marouf et al.* [1986] for use in radio occultation studies of planetary rings. In that case, the observation line and the ring plane are separated by vacuum so that the EM wave emerging from the rings can be reconstructed exactly from the original observations through application of a standard Huygens-Fresnel diffraction integral. Our formula for backward propagation, (21), is the frequency domain equivalent of the Fresnel filter derived by *Marouf et al.* [1986] to implement this step. Because the rings of Saturn and Uranus are extremely thin, the back-propagated field is free of appreciable diffraction effects, and its phase and amplitude give a direct measure of the modulation imposed by the ring material. In this way, *Marouf et al.* [1986] were able to obtain profiles of ring opacity at radial resolutions that are typically 1–2 orders of magnitude smaller than the Fresnel scale, revealing a remarkable array of sub-Fresnel-scale structure including extremely sharp edges, narrow ringlets, bending and density waves, and wakes of embedded satellites.

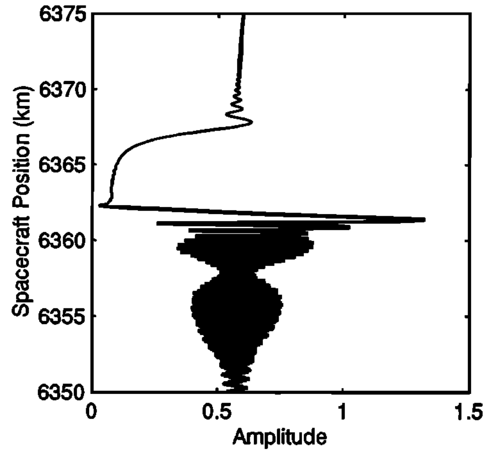

Figure 10. MPS calculations of received signal amplitude for the terrestrial case. The small-scale structure of size 250 m causes noticeable diffraction effects for the observation position range of 6360–6370 km. The smaller fluctuations near 6350 km are artifacts of the forward simulation. Note that refractive defocusing has reduced the average amplitude by about 40%.

The main obstacle to adapting this procedure to atmospheric occultations is that a planetary atmosphere is an extended medium, while a planetary ring is essentially planar with negligible thickness. This difference introduces some conceptual difficulties, and an important distinction needs to be made. Equation (21) assumes vacuum propagation, whereas the plane $z = b$ to which we back propagate is actually within the occulting atmosphere. Hence the field at $z = b$ obtained with (21) is not the same as what actually occurred at this location. This is not a problem per se, since our goal is not to reconstruct the true field at any key location in the experiment. We are attempting instead to filter the data via (21) in such a way that $\alpha(a)$ can be extracted with little or no interference from diffraction effects.

The simplest case to consider is a radio occultation by an extremely tenuous atmosphere, such as Triton's. Its atmosphere can be modeled accurately as a thin, phase-changing screen, so that the procedure used to remove diffraction effects from radio occultation measurements of planetary rings is directly applicable. (This corresponds to $b = 0$ in our back-propagation algorithm.) Radio occultation measurements of Triton's atmosphere obtained with Voyager 1 show clear diffraction effects caused by the surface, which were successfully removed from the data using the ring methodology [*Tyler et al.*, 1989]. This proce-

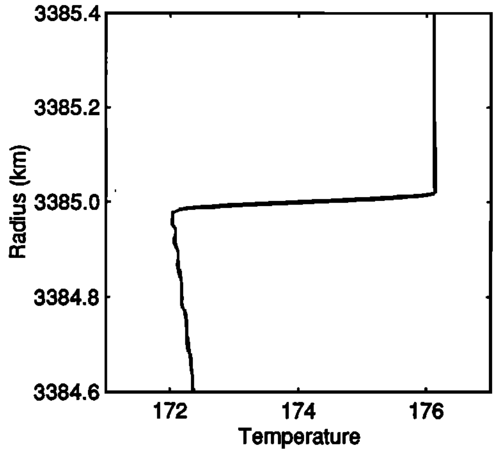

Figure 11. Temperature profile retrieved through back propagation (solid curve). Model atmosphere used in forward simulations (dashed curve) was Mars-like with a 40-m-scale structure.

dure worked well for the Triton data in that the back-propagated field contained no noticeable diffraction fringes and the surface appeared as a sharp knife-edge. *Tyler et al.* [1989] then deduced a number of useful atmospheric parameters through analysis of the back-propagated field, including the first and most accurate estimate of surface pressure (~1.6 Pa). However, no sub-Fresnel-scale structure was actually observed in Triton's atmosphere.

We tested the back-propagation inversion algorithm for the atmosphere of Mars using results from MPS forward simulations described above and shown in Figures 7 and 8. Although the refractive bending on Mars is ~200 times larger than on Triton, the optimum value for b is still very small (~0.7 km), and b can safely be set to zero without seriously degrading the results. The amplitude of the field after back propagation is close to unity, and both the amplitude and phase exhibit no significant diffraction effects. The retrieved temperature profile fits the actual profile remarkably well as shown in Figure 11 for the case where Δr = 40 m. The back-propagation method clearly overcomes the diffraction limit to resolution in that a structure 6 times smaller than the Fresnel scale is retrieved accurately. This represents a twelvefold enhancement over the resolution achieved through Abel inversion.

We found that the back-propagation method also performs well in simulated occultations by the denser terrestrial atmosphere, in which the refractive bending was ~50 times larger than on Mars. We began with the simulated data obtained by the MPS method for a model atmosphere with a 250-m-scale structure (cf. Figures 3 and 10). Figure 12 shows the amplitude of the field after back propagation for several different choices for b in (21). Residual diffraction effects are minimized when $b \approx$ 110 km; examination of phase data leads to the same conclusion. One other point of interest in these plots is the presence of oscillations at lower altitudes, which are again an artifact of the MPS forward simulations. These were also seen in the field at the observation line (cf. Figure 10). Back propagation reduced the magnitude of the artifacts considerably but did not remove them completely. However, these artifacts do not represent a limitation of the back-propagation retrieval algorithm since they would of course not be present in real occultation measurements.

Figure 13 shows bending angle versus impact parameter computed from the back-propagated field when b = 110 km. The retrieved temperature profile appears in Figure 14. The temperature errors in the reconstruction are less than 0.4 K within the small-scale structure. As in the Martian example, the back-propagation method appears capable of accurately resolving sub-Fresnel-scale atmospheric structure.

Discussion

Given the variation of α with a in Figure 13, a receiver at sufficient distance from the occulting

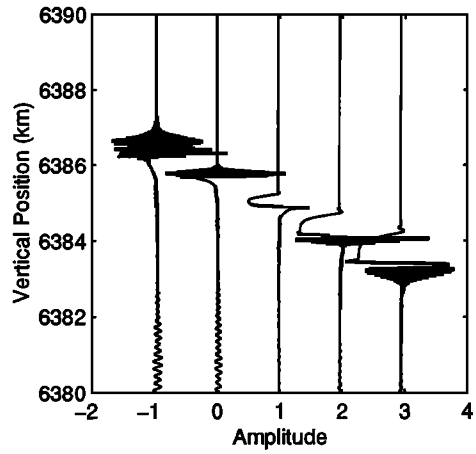

Figure 12. Amplitude of the back-propagated field for the terrestrial simulations (cf. Figure 10). Curves correspond to different values of b in (21) (0, 55, 110, 165, and 220 km from left to right). Amplitude scale applies to central curve (b = 110 km). Others have been offset by integer multiples of 1 for comparison. Diffraction removal is most effective when b = 110 km.

atmosphere will observe "multipath propagation," wherein several distinct signals with different values of α and a arrive simultaneously at the spacecraft. This corresponds to ray crossing in the geometrical optics view. We found through spectral analysis of the complex field at the observation line that multipath effects were indeed present in the forward simulation described above for the terrestrial atmosphere. It is possible in principle to track the multiple signals simultaneously because spacecraft motion causes each to have a different Doppler-shifted frequency. However, this can be difficult in practice due to wide differences in the amplitude of the various modes, to interference from thermal and oscillator noise, and to the presence of diffraction effects (spectral broadening). In this regard, the back-propagation method provides a natural means for deciphering multipath propagation. The initial step of backward propagation eliminates ray crossing while at the same time removing both diffraction effects and refractive defocusing (cf. Figures 12 and 13).

We explored the limitations of the back-propagation method by conducting a series of terrestrial simulations in which we varied the magnitude of the small-scale change in refractivity, ν_s, while keeping other parameters fixed at the values given in Figure 3. For each value of ν_s a temperature profile was retrieved using the back-propagation method and compared with the actual profile used in the forward MPS calculations. The maximum temperature error was less than 0.2 K when $\nu_s = 4 \times 10^{-6}$, increasing to nearly 0.4 K for $\nu_s = 10^{-5}$ (Figure 14), and 2 K for $\nu_s = 1.4 \times 10^{-5}$. When $\nu_s = 1.8 \times 10^{-5}$, the method fails. In that case, multipath is present for all choices of the parameter b, and a more elaborate retrieval algorithm is required.

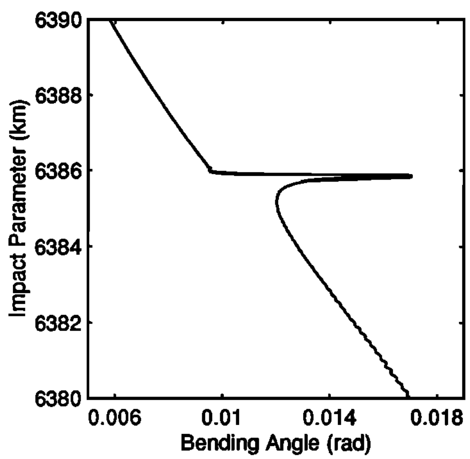

Figure 13. Bending angle versus impact parameter computed from the back-propagated field when b = 110 km in the terrestrial simulation. Diffraction fringes are essentially absent.

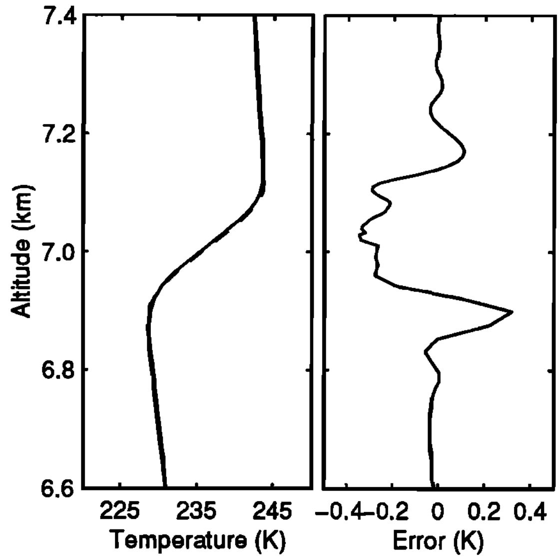

Figure 14. (left) Temperature profile retrieved through back propagation (solid curve) compared with model used in MPS calculations (dashed curve). (right) Difference between two temperature profiles on left.

Critical refraction imposes a fundamental limitation on the refractivity gradient that can be retrieved from radio occultation measurements through this or any other method. This event occurs when the vertical gradient of ln μ exceeds $1/r$ at radius r. The behavior of electromagnetic waves in this region of the atmosphere is analogous to total internal reflection at a dielectric interface, rendering the critical region inaccessible to remote sounding. For the terrestrial simulations described above, critical refraction occurs when $\nu_s = 2.3 \times 10^{-5}$. Comparing this constraint with results from our simulations, we see that despite its limitations, the back-propagation method is within striking distance of the theoretical limit of the radio occultation technique.

We assumed throughout this paper that the refractive index in the atmosphere under study is a function of radius alone. When this condition is violated, it is generally not possible to retrieve unambiguous atmospheric profiles from a single radio occultation experiment. Departures from spherical symmetry can also hamper attempts to retrieve profiles at fine vertical resolution. For example, in the presence of significant topographic variations the atmospheric boundary layer adjacent to the surface of a terrestrial planet will follow the undulating terrain. Fine-scale structure of this sort is of course difficult to resolve with "limb-sounding" observations, such as radio occultations. As a first approximation, the horizontal coherence scale along the direction of propagation (the z direction in Figure 6) must be $\sim 2(2r\Delta r)^{1/2}$ or greater before structure of radial scale Δr can be resolved accurately; this is ~30 km for Mars when $\Delta r = 40$ m and ~110 km for Earth when $\Delta r = 250$ m. Hence the vertical resolution that can be achieved through Abel inversion or back propagation should be regarded as an instrumental capability that cannot always be achieved in practice.

A number of other practical issues must also be investigated before the performance of the back-propagation method is fully understood. The vertical resolution that can be achieved in a particular experiment depends on factors including signal-to-noise ratio, instability of reference oscillators, nonideal experiment geometry, and trajectory uncertainty [cf. *Marouf et al.*, 1986]. Their impact on atmospheric profiles retrieved through back propagation will be the subject of future work. However, experience with radio occultation measurements of planetary rings [cf. *Marouf et al.*, 1986] suggests that sub-Fresnel-scale vertical resolution will be feasible in well-designed experiments, such as those planned with Mars Global Surveyor [*Tyler et al.*, 1992].

Acknowledgments. This work was made possible through support from NASA (contracts JPL-957626 of the Mars Global Surveyor Project and JPL-958736 of the Galileo Project) and NSF (grant ATM-9223570). V. R. Eshleman and G. L. Tyler provided useful comments during numerous discussions.

References

Born, M., and E. Wolf, *Principles of Optics*, 6th ed., corrected, Pergamon, Tarrytown, N. Y., 1986.

Bracewell, R. N., *The Fourier Transform and its Applications*, 2nd ed., revised, McGraw-Hill, New York, 1986.

Brigham, E. O., *The Fast Fourier Transform*, Prentice-Hall, Englewood Cliffs, N. J., 1974.

Cohen, M. H., High resolution observations of radio sources, *Annu. Rev. Astron. Astrophys.*, *7*, 619–664, 1969.

Eshleman, V. R., The radio occultation method for the study of planetary atmospheres, *Planet. Space Sci.*, *21*, 1521–1531, 1973.

Eshleman, V. R., Pluto's atmosphere: Models based on refraction, inversion, and vapor-pressure equilibrium, *Icarus*, *80*, 439–443, 1989.

Fjeldbo, G., and V. R. Eshleman, The atmosphere of Mars analyzed by integral inversion of the Mariner IV occultation data, *Planet. Space Sci.*, *16*, 1035–1059, 1968.

Fjeldbo, G., and V. R. Eshleman, Atmosphere of Venus as studied with the Mariner 5 dual radio-frequency occultation experiment, *Radio Sci.*, *4*, 879–897, 1969.

Fjeldbo, G., A. J. Kliore, and V. R. Eshleman, The neutral atmosphere of Venus as studied with the Mariner V radio occultation experiments, *Astron. J.*, *76*, 123–140, 1971.

French, R. G., and R. V. E. Lovelace, Strong turbulence and atmospheric waves in stellar occultations, *Icarus*, *56*, 122–146, 1983.

Goodman, J. W., *Introduction to Fourier Optics*, McGraw-Hill, New York, 1968.

Haugstad, B. S., Effects of the inhomogeneous background on radiation propagating through turbulent planetary atmospheres, *Radio Sci.*, *13*, 435–440, 1978.

Hinson, D. P., and J. A. Magalhães, Equatorial waves in the stratosphere of Uranus, *Icarus*, *94*, 64–91, 1991.

Houghton, J. T., *The Physics of Atmospheres*, Cambridge Univ. Press, New York, 1977.

Howard, H. T., et al., Galileo radio science investigations, *Space Sci. Rev.*, *60*, 565–590, 1992.

Kak, A. C., and M. Slaney, *Principles of Computerized Tomographic Imaging*, IEEE, New York, 1988.

Knepp, D. L., Multiple phase-screen calculation of the temporal behavior of stochastic waves, *Proc. IEEE*, *71*, 722–737, 1983.

Kursinski, E. R., et al., Initial results of radio occultation observations of Earth's atmosphere using the Global Positioning System (GPS), *Science*, *271*, 1107–1109, 1996.

Lindal, G. F., H. B. Hotz, D. N. Sweetnam, Z. Shippony, J. P. Brenkle, G. V. Hartsell, R. T. Spear, and W. H. Michael Jr., Viking radio occultation measurements of the atmosphere and topography of Mars: Data acquired during 1 Martian year of tracking, *J. Geophys. Res.*, *84*, 8443–8456, 1979.

Marouf, E. A., G. L. Tyler, and P. A. Rosen, Profiling Saturn's rings by radio occultation, *Icarus*, *68*, 120–166, 1986.

Martin, J. M., and S. M. Flatté, Intensity images and statistics from numerical simulation of wave propagation in 3-D random media, *Appl. Opt.*, *27*, 2111–2126, 1988.

Owen, T., The composition and early history of the atmosphere of Mars, in *Mars*, edited by H. H. Kieffer, B. M. Jakosky, C. W. Snyder, and M. S. Matthews, pp. 818–834, Univ. of Ariz. Press, Tucson, 1992.

Tatarskii, V. I., *The Effects of the Turbulent Atmosphere on Wave Propagation*, Natl. Tech. Inf. Serv., Springfield, Va., 1971.

Tyler, G. L., Radio propagation experiments in the outer solar system with Voyager, *Proc. IEEE*, *75*, 1404–1431, 1987.

Tyler, G. L., et al., Voyager radio science observations of Neptune and Triton, *Science*, *246*, 1466–1473, 1989.

Tyler, G. L., G. Balmino, D. P. Hinson, W. L. Sjogren, D. E. Smith, R. Woo, S. W. Asmar, M. J. Connally, C. L. Hamilton, and R. A. Simpson, Radio science investigations with Mars Observer, *J. Geophys. Res.*, *97*, 7759–7779, 1992.

Ware, R., et al., GPS sounding of the atmosphere from low Earth orbit: Preliminary results, *Bull. Am. Meteorol. Soc.*, *77*, 19–40, 1996.

Zurek, R. W., J. R. Barnes, R. M. Haberle, J. B. Pollack, J. E. Tillman, and C. B. Leovy, Dynamics of the atmosphere of Mars, in *Mars*, edited by H. H. Kieffer, B. M. Jakosky, C. W. Snyder, and M. S. Matthews, pp. 853–933, Univ. of Ariz. Press, Tucson, 1992.

D. P. Hinson and E. T. Karayel, Center for Radar Astronomy, Stanford University, Stanford, CA 94305-9515. (e-mail: hinson@nova.stanford.edu; karayel@nova.stanford.edu)

(Received June 4, 1996; revised October 15, 1996; accepted October 21, 1996.)